

Visible and invisible mirages: comparing inferior mirages in the visible and thermal infrared

Michael Vollmer,^{1,*} Joseph A. Shaw,² and Paul W. Nugent²

¹Brandenburg University of Applied Sciences, 14770 Brandenburg, Germany

²Electrical and Computer Engineering Department, Montana State University, Bozeman, Montana 59717, USA

*Corresponding author: Vollmer@fh-brandenburg.de

Received 29 July 2014; accepted 23 August 2014;
posted 24 September 2014 (Doc. ID 217579); published 21 November 2014

Visible (VIS)-light and thermal infrared (IR) inferior mirages in the 8–14 μm waveband have been observed simultaneously for the takeoff and landing of various airplanes at distances of several kilometers. Similarities as well as differences between the VIS and IR mirages are discussed. © 2014 Optical Society of America

OCIS codes: (010.1290) Atmospheric optics; (010.4030) Mirages and refraction; (110.3080) Infrared imaging.

<http://dx.doi.org/10.1364/AO.54.000B76>

1. Introduction

Mirages are among the most documented atmospheric optical phenomena since they are rather frequent and are easy to observe and record [1–3]. Mirages are formed when light rays bend as they propagate through regions where the atmospheric refractive index varies significantly from its usual state, causing an observer to see additional images of an object located above or below its usual apparent location [4]. A superior (higher) mirage appears above the erect image of the object, whereas an inferior (or lower) mirage appears below the erect image of the object [4–9]. Either type requires strong deviation from the normal atmospheric temperature profile, which cools with increasing altitude at a rate of approximately $7^\circ\text{C}/\text{km}$. Because of its higher number density, cold air has a higher refractive index than warm air. Therefore, warm air overlying cool air can cause light rays originally directed above an observer's head to bend downward, creating an image of the object floating in the air above its usual location and flipped vertically. This superior mirage

situation occurs often over the ocean, resulting in upside-down images of distant boats or islands that appear to be in the sky just above the horizon [4,5]. The same situation also occurs with strong temperature inversions in polar regions, giving rise to images of upside-down and distorted mountains that appear to float in the air [8].

If the situation is reversed, so that a layer of very warm air lies below cooler air above, light rays from the sky above the horizon can be refracted upward to cause an observer to see a region of sky superimposed over the underlying surface. This is the common inferior mirage effect, in which occupants of a car can see what appears to be a lake or puddle of water lying on the road ahead of them [3,5]. For this to occur, the atmospheric temperature gradient must change with height. All mirages generally produce distorted images that change over time because of turbulence, or even atmospheric waves [10,11].

The science of visible (VIS) mirages has been used to resolve mysteries involving missing islands [12] or unidentified optical phenomena [13], and to explain historical mirage observations [14]. The same scientific principles have been applied to inverse problems to recover atmospheric temperature profiles from mirage images [15–19].

The fascination for mirages and other atmospheric optics phenomena stems primarily from their easy observability with the naked eye. However, investigation of such phenomena in adjacent spectral regions using suitable detectors can prove similarly fascinating for experimental physics. For example, in the 1970s, cameras with film sensitive to near-infrared (NIR) light were used to record the first observed IR rainbows in the wavelength range of 800–900 nm [20], and modern digital single-lens reflex cameras easily record images in the NIR spectral range between approximately 700 and 1000 nm [21].

At even longer wavelengths, thermal IR imaging also is becoming rapidly more accessible, in both mid-wave IR (MWIR, $\sim 3\text{--}5\ \mu\text{m}$) and long-wave IR (LWIR, $\sim 8\text{--}14\ \mu\text{m}$) wavelength bands [22]. Thermal IR imaging has been applied to studies of natural phenomena that range from measuring cloud statistics [23] or estimating aerosol optical depth from earthbound lunar measurements [24], to characterizing emission from the sea surface [25], for which the surface roughness varies strongly with both wind speed and air-sea temperature difference [26]. Among more conventional atmospheric optics phenomena, glories have been observed at wavelengths up to $3.7\ \mu\text{m}$ from high-altitude aircraft [27].

There are only a limited number of previous investigations of IR mirages. One experiment used a modulated CO_2 laser transmitted across an 8.5 km path toward a point detector with telescope optics to study distortions of atmospheric boundary layers in the LWIR region [28]. Thermal IR images for the 8–12 μm wavelength band and accompanying VIS images of inferior mirages were reported for an arid region in India, showing that LWIR mirages occurred along with VIS mirages when trucks were imaged through a telescope at ranges of 4–5 km [29]. A more complete study of thermal IR mirages was by Lehn [30] who modeled a 22 min sequence of images acquired at Wallops Island (Virginia, USA) with a ground-based IR camera, viewing a thermal source mounted 22 m above mean sea level on a ship. The IR camera had 256×256 pixels in a $0.48^\circ \times 0.48^\circ$ field of view (FOV) and operated in the MWIR band of 3.9–5.1 μm . He found that the model reproduced key features of the MWIR images if he assumed that gravity waves were propagating along a small temperature inversion in a slightly sloping atmosphere. Other studies have focused on analysis and progressively more sophisticated models of thermal IR mirages over the ocean [31–33].

Previous IR mirage observations were limited in image quality and resolution, but have been studied and modeled with significant success. Furthermore, a comparison of VIS and LWIR mirages is still missing. This paper helps to fill these gaps by presenting simultaneous VIS and LWIR imagery of inferior mirages recorded while observing airplanes taking off and landing at the Bozeman-Yellowstone International Airport at Gallatin Field, located northwest of Bozeman, Montana, USA.

Relative to previous IR mirage reports, this study benefits from higher-resolution images in both the IR and VIS. Even still, whereas current VIS-wavelength digital cameras routinely offer more than 10 megapixels and a large variety of telephoto lenses, LWIR cameras currently have typically 1 megapixel or less, with the best readily available resolution being 0.3 megapixels ($\sim 640 \times 512$ pixels). Furthermore, the long-focal-length optics required for mirage studies are not common in IR imaging since most IR imaging applications require wider-angle optics, with FOVs in the range of $10^\circ\text{--}45^\circ$ (e.g., in applications such as building thermography, electrical equipment monitoring, predictive maintenance, etc., as summarized in [22]). As a consequence, IR cameras with long-focal-length lenses are much more expensive, and hence, less widespread than VIS ones. This may explain why IR mirages are not reported more often. Nevertheless, recent development of increasingly compact thermal IR cameras at lower cost, with a larger range of IR optics, has increased the number of studies relying on such thermal imagery [23,24].

The mirage study reported here uses a compact LWIR camera (FLIR Tau 640), operating in the 7.5–13.5 μm band with 640×512 pixels and a $3.1^\circ \times 2.5^\circ$ FOV, mounted inside a small reflective telescope [34]. The remainder of this paper is organized as follows: first, we discuss the refractive index of air and infer the expected differences between VIS and IR mirages. Next, we present experimental VIS and LWIR mirage images for airplanes during takeoff and landing. Finally, we discuss the data with regard to similarities and differences between the VIS and LWIR mirages.

2. Index of Refraction of Air in the VIS and Thermal IR

Mirages are caused by gradients in the index of refraction such that incident waves—if described as light rays—are forced to follow curved paths. The changes of index of refraction are induced by hot surfaces in contact with colder air layers: due to diffusion and slow mixing processes, gradients can build up under appropriate conditions. In the following text, we will only refer to simple inferior mirages observed on sun-heated roads or airstrips with horizontal distances below 3.5 km. Therefore, we need not discuss any mirage effects for longer distances with air layers leading to ducts [7,11].

To find out whether differences are to be expected between VIS and IR mirages, we discuss the index of refraction of air. A number of literature data and models are available, with small differences. Since we are interested only in respective changes between VIS and IR, and the features are similar for different data sets, we arbitrarily choose two sets of data. The data for the index of refraction for VIS light is based on a dry air model after Penndorf and Edlén [35,36] for a standard pressure of 1013.25 hPa and a temperature of 15°C . Penndorf [35] also estimated changes induced by moisture, which would just lead to offsets of the order of 10^{-7} . The low CO_2 content of only

300 ppm is not important for the VIS range and would only induce an additional small offset.

Figure 1 shows the real part of the index of refraction for dry air [36] at five different temperatures, plotted as a function of wavelength from the UV to the LWIR. The dependence on temperature and pressure follows approximately

$$n - 1 \propto \frac{p}{T}. \quad (1)$$

First of all, dispersion effects between the blue and red edges of the VIS range are very small (around 7×10^{-6}). Assuming that for visual perception the blue and red extend between 450 and 650 nm, the dispersion would be even lower (around 4×10^{-6}). By contrast, changes due to temperature gradients are more pronounced. For a given wavelength, a temperature change of 15°C induces an index change of around 10^{-5} . This general behavior explains why mirages in air do not usually show dispersion effects due to $dn/d\lambda$ (whereas experimental ones in liquids may do so [9]), but instead, temperature gradients dn/dT dominate.

We note that the approximate model for the VIS range underlying Fig. 1—although sufficient for our discussion here—is quite simple and has been improved considerably (see, e.g., [37,38]). However, it completely fails for the thermal IR range since it does not include any rovibrational molecular excitations due to CO_2 for dry air. In addition, air in the atmosphere is never dry, but always includes some water vapor, which also shows pronounced rovibrational excitations. As seen in Fig. 1, there is much

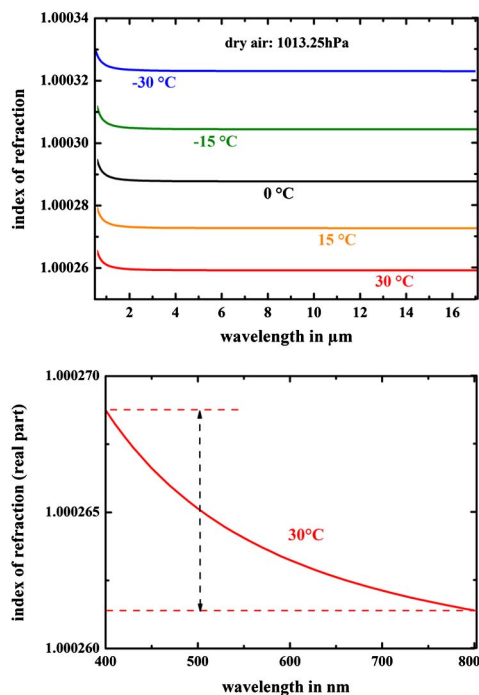


Fig. 1. (Top) Index of refraction of dry air from the model of Edlen [36]. (Bottom) Index of refraction of dry air at 30°C zoomed in to emphasize the dispersion in the VIS wavelength range.

less dispersion in the IR than in the VIS range, whereas the temperature gradient effects stay more or less the same; i.e., according to this plot, mirages should be easily observable in the thermal IR, too. The results in Fig. 1 can be easily extended to other pressures using Eq. (1).

To illustrate how the index profile changes in more realistic air, Fig. 2 depicts the computed index of refraction spectra for the thermal IR range, including the rovibrational excitations of CO_2 and H_2O vapor (after [39]). The computations are based on the Hitran 2000 database with more than 58,000 lines from CO_2 and H_2O between 400 nm and $25 \mu\text{m}$. In addition to 365 ppm of CO_2 and 0.5% water vapor, N_2 , O_2 , Ar, Ne, CH_4 , O_3 , and CO were included. The other main difference is the chosen total pressure of the air (752.9 hPa), which corresponds to the location of the Very Large Telescope at a height of around 2635 m above sea level. Again, the resulting offset with pressure follows more or less from Eq. (1). Figure 2 shows the same general form of n with a change $dn/d\lambda$ due to electronic UV excitations of the air molecules, and, in addition, there are pronounced rovibrational excitations of CO_2 and H_2O in the thermal IR around 2.7, 4.3, 5.5–7.5 μm , and above 15 μm . These induce local changes of the index of refraction in adjacent spectral regions (for an improved IR model of the refractive index, see [40]).

Commercial IR thermal imaging systems typically operate within the atmospheric windows: either the MWIR window of approximately 3–5 μm or the LWIR window of approximately 8–14 μm [22]. The MWIR band includes the prominent CO_2 absorption around 4.2–4.3 μm . Therefore, such cameras usually have to

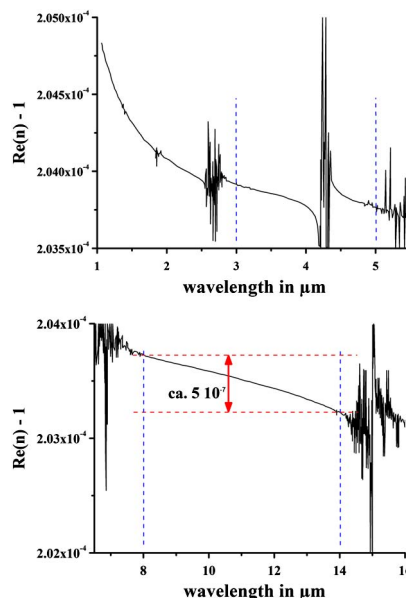


Fig. 2. Index of refraction of moist air in MWIR (top) and LWIR (bottom) for a model with given number densities of gases, referring to $p \approx 750 \text{ hPa}$ and $T \approx 12^\circ\text{C}$ (after [39]). The vertical lines indicate the wavelength ranges of typical commercial IR cameras. Not all line features are resolved in this graph.

effectively correct for CO₂ absorption. We, therefore, chose to use a LWIR camera operating in the 8–14 μm band, which avoids many atmospheric absorption features (Fig. 2, bottom). The absolute value of n varies slightly between the VIS and NIR wavelengths (about 3% difference between 0.5 and 10 μm at STP); it is, however, the gradients in temperature and pressure that determine refraction [28]. For the conditions of the data in Fig. 2 (753 hPa), dispersion across the detected range from 8 to 14 μm amounts at most to about 5×10^{-7} , less than that in the VIS range. Therefore, any dispersion effect is negligible when observing IR mirages. As a consequence, we only expect temperature-induced index gradients, such that IR mirages should be similar to VIS mirages.

Assuming that the conditions for inferior mirages are given in the form of temperature-induced variations of the index of refraction (e.g., due to hot air near a hot ground on a summer day), one may still face problems in observing mirages if the contrast is poor. For VIS mirages, the usual contrast arising from differences in colors or brightness can be strongly decreased by haze, in particular with long distances between objects and the observer. However, in the thermal IR range, one observes a thermal contrast, which arises from either differences in the surface temperatures of the objects observed or differences in emissivity. In addition, thermal reflection of very hot or cold objects (e.g., the cold sky) from metallic surfaces can give rise to additional features. Since IR radiation is attenuated by absorption and scattering, the large distances required for mirage observations pose an additional problem: accurate measurement of temperatures or radiances in the mirage scene would require compensation for a continually changing atmospheric path during the observation of transient phenomena like airplane takeoffs or landings. Therefore, our mirage observations, although actually recorded with a radiometrically calibrated IR camera, are only analyzed qualitatively with regard to mirage features. Finally, because optical scattering by small haze particles decreases strongly with wavelength, visibility is better in the IR than in the VIS range [22] and LWIR mirages may be more easily observable.

3. Equipment and Measurement Locations

Experiments were conducted in August 2012 for several street mirages with cars as objects at distances up to 600 m, but mostly for landings and takeoffs of airplanes at the Bozeman-Yellowstone International Airport at distances up to 3.5 km. Similar to recordings of visual mirages, this was best done with narrow-FOV optics. As shown in Fig. 3, we used a telescope-mounted LWIR camera system from Polaris Sensor Technologies, Inc. [34]. This system consists of a mirror telescope with a 17 cm aperture and a 200 mm effective focal length, combined with a microbolometer FLIR Tau 640 LWIR camera (640 × 512 pixels, 17 μm pitch), providing a $3.1^\circ \times 2.5^\circ$



Fig. 3. Telescope-mounted LWIR camera used for observing IR mirages.

FOV. The camera responds in the 7.5–13.5 μm spectral band and outputs images at 30 frames per second (fps). The USB-powered camera requires only 1.2 W of electricity, which allows field operation.

At the airport, IR and VIS images and videos of mirages were recorded simultaneously. The VIS camera was a Nikon D300 with a Nikon 80–400 mm zoom lens, which recorded high-resolution photos at 1 fps. In addition, a Panasonic video camera recorded standard 30 fps VIS video. Figure 4 shows the experimental setup of the cameras for the airport observations. The IR camera (left) and VIS cameras (right) were mounted on tripods on top of cars. Whenever a take-off or landing was taking place, a digital video recorder was used to record the 8 bit analog output of the IR camera at 30 fps. The IR camera also was used to capture a variety of single images with full 14 bit resolution.

IR mirages were observed successfully and were recorded during the street and airport experiments. Here we present the results recorded on 6 and 7 August 2012 at the airport since they were associated with much stronger VIS mirages. Figure 5 shows a Google Earth image of the airport, located northwest of Bozeman, Montana, USA. Our observation position just beyond the southeast end of the 2.8 km runway was approximately 3.4 km from the northwest end of the runway, as indicated by the thin red line in the figure, estimated with the distance tool in Google Earth [41]. Observation from the opposite northwest side was unfortunately not possible since the street behind the airport was further away and was at a lower elevation, such that only part of the runway could be seen. During an overall



Fig. 4. Airport mirage imaging experiment in August 2012 with an IR camera (left) and VIS cameras (right).



Fig. 5. Google Earth image (© 2012 Google) of the Bozeman-Yellowstone International Airport at Gallatin Field. The distance from the beginning of the runway to the observation point (red line) was 3.40 km.

five- to six-hour period, 4 landings and six takeoffs were successfully recorded simultaneously with the VIS and IR cameras out of around 20 events overall.

Because of prevalent southeasterly winds, all planes recorded were either starting or landing from the northwest corner (airplanes always take off or land into the wind). Therefore, they were either accelerating during takeoff or decelerating during landing, all while approaching the cameras directly. This, unfortunately, meant that we could not observe the hot engine exhaust as the most obvious heat signature of air planes from behind (e.g., Fig. 9.33 in [22]). However, as is shown next, IR mirages were still easily recognizable.

There are no fundamental differences between the mirages observed for takeoff and landing. The observed angular ranges were determined by the observation distance (1–3.4 km) and airplane size. Bozeman air traffic includes many short-range regional jets carrying fewer than 100 passengers, as well as a few medium-range jets. Regional jets typically have a wing span near 25 m and height near 8 m. By contrast, medium-range jets (e.g., Boeing 737 or Airbus 318-321 type) have a larger average wing span of around 30 m and an average height of around 12 m. A plane of 25 m wing span at distances of 3.4 and 2 km would present angular widths of 0.4° and 0.7° , respectively, which for the telescope-mounted IR camera's 3.1° FOV would correspond to around 90–140 pixels. The angular range of the mirage itself is related to the height of the plane, which is around one-third of its wing span. Therefore, angular ranges between 0.1° and 0.25° could be observed, which could be nicely resolved with typically 20–50 pixels of the telescope-mounted IR camera covering the mirage vertical extension.

4. Results and Discussion

To be sure that mirage conditions existed, we always detected VIS mirages simultaneously. Once VIS

mirages were observable, we could safely assume that IR mirages were also present.

A. VIS Mirages Observed during Takeoff and Landing

A large number of VIS mirages were detected for the airplane takeoffs and landings, from which we show a few examples. Figure 6 shows four photographs of the takeoffs of two airplanes: a regular jet [Figs. 6(a)–6(c)] and a regional jet [Fig. 6(d)]. Initially, at the largest distance of about 3.4 km [Figs. 6(a) and 6(b)], typical inferior mirages can be observed. For the distant plane [Figs. 6(a) and 6(b)], the lower parts of the plane, such as the wheels, are hidden. They lie below the so-called vanishing line [1], i.e., there is no optically allowed light path from the wheels to the observer. The vanishing line, related to a vanishing horizon distance, can be regarded as the mirror line below which the inverted image of the inferior mirage can be seen. The position of this vanishing line depends on the position of the observer, the vertical profile of the index of refraction within the atmosphere, and the geometry. In our

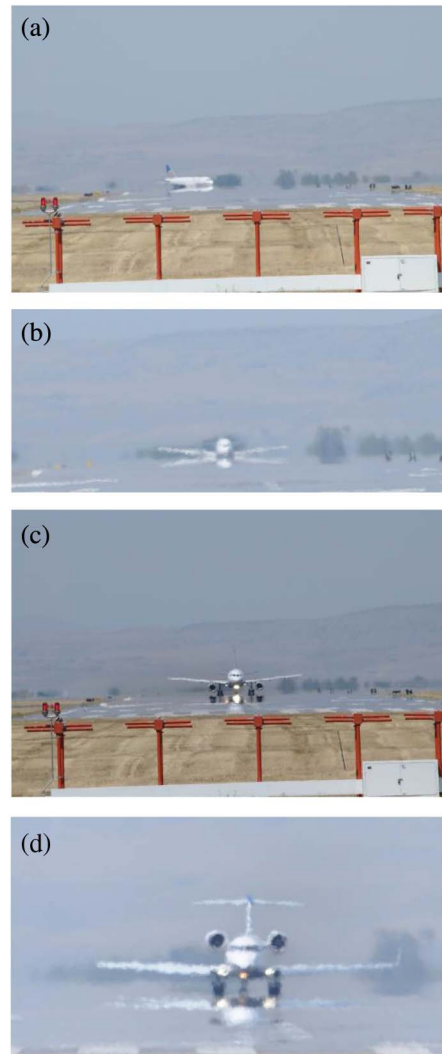


Fig. 6. Photographs of airplane takeoffs recorded with Nikon D300 and a 400 mm lens: (a)–(c) medium-range jet; (d) regional jet.

case, the runway is not flat, but is slightly curved, with a convex shape that leads to a vanishing line horizon that is closer than the length of the runway. Therefore, we can easily observe inferior mirages even at camera heights of 2.5 m above the ground. The upward bending of the wings results in an apparent four-wing structure. As the plane approached the observer, and came closer than the vanishing line horizon, formerly hidden objects such as headlights, engine, and wheels became visible in the mirage [Fig. 6(c)].

The contrast in Fig. 6 results from differences in scene radiance, related to properties of the objects in the scene. In this case, the airplane provides the highest- and lowest-radiance elements in the scene: the brightest areas are the headlights and the white painted airplane body, and the darkest areas are the turbine openings (cavity effect) and the dark rubber tires. The radiance of sunlight scattered from the background landscape and from the air path between the scene and the observer lies in between these two extremes. As a result, nice VIS mirages can be observed with rather good contrast.

B. IR Images of Planes: Characteristics of and Differences between Takeoff and Landing

There are obvious differences between the VIS and LWIR images of planes, and the contrast in IR radiation from objects in a scene differs from the contrast in VIS radiation appreciably. For the LWIR band, scattered sunlight can be neglected compared with the thermal radiation of the objects [22]. Therefore, IR contrast is caused by, first, changes in the surface temperatures of the observed opaque objects; second, variations of the emissivity of the objects; and third, reflection of background radiation from hot or cold objects into the FOV. During takeoff or landing, the various contributions can vary. For example, very prominent heat sources are the wheels, which heat up from friction with the runway. The heating is most pronounced during landing, when the cold wheels first touch the ground. In our experiments, the thermal signatures of the four individual tires of a landing airplane could be detected easily one after the other. Also, a slight mirage effect was observed to cause the tires to appear elongated.

A second prominent heat source is the hot exhaust gas from the engines. However, in the examples discussed, we only recorded images from the front due to the prevailing wind conditions. Therefore—although detectable—the temperature contrast between the engines and their surroundings is not as pronounced as it may be when looking from behind the plane [22]. In addition, the finite width of the hot exhaust gases is small and absorption due to the gas, mostly CO₂ and H₂O vapor as combustion end products, is relatively small in the LWIR band; therefore, the optical thickness of the gas plume is low, so that the apparent temperatures will not resemble the actual gas temperature. In some cases, landing planes were

observed when leaving the air field and turning toward the terminal. In these cases, the hot gas plume could be seen from the side and could be detected easily. By contrast, the covers of the headlights did not heat up much and were not usually observed.

Another good source for IR contrast is emissivity variation. The outer parts of the hull and wings usually consist of metallic surfaces that are characterized by low emissivity (only part of them is covered by higher-emissivity paint). To avoid turbulence and reduce fuel consumption, these surfaces tend to be flat. This means, however, that they also reflect surrounding radiance. For example, looking from the front, one can readily detect reflections of the cold sky above the plane from the tops of the hull and wings, whereas the lower hull reflects radiation from the sun-heated runway. Finally, the landscape behind and on the sides of the plane, as well as the runway itself, all emit thermal radiation that defines the background level. A detailed analysis would also have to include thermal radiation emitted by the atmosphere between the object and the observer.

For our discussion, we neglect some of these details, but mention one advantage of IR images compared with VIS images, which relates to the atmosphere. Since observations are made over distances of several kilometers, atmospheric haze can be an issue at VIS wavelengths. However, LWIR radiation is much less affected by atmospheric scattering [22], so it may be possible to observe objects and mirages for hazy atmospheres at large distances in the IR when the VIS contrast is not sufficient. Unfortunately, the background radiance in the LWIR band was quite high on the hot summer days of these observations. Therefore, the thermal contrast was limited, and for this reason, we have presented images here in gray scale. In addition, the transient effects are illustrated in video sequences available as multimedia supplements to this paper.

Finally, there is one major difference between the observations for planes during takeoff and landing. The angular ranges from the far end of the runway (3.4 km distance) to the point of takeoff for departing aircraft or the point of turning toward the terminal for arriving aircraft (between 1 and 2 km, depending on aircraft) are the same; however, landing aircraft are slowest at the nearest point and departing aircraft are fastest there. Therefore, the time periods for observing nice mirages at the closest distances differ, so arriving planes offer better observation conditions. For a 1/30 s integration time of the IR camera, each image blurs the motion while the airplane travels a distance $s = v \times t$, where v is velocity and t is the 1/30 s integration time. For a plane landing with velocity near 50 km/h (~14 m/s), the blur distance is 0.5 m, whereas for a plane taking off with velocity near 300 km/h (83 m/s), the corresponding distance increment is 2.8 m. Since mirages are always blurred by turbulence anyway, the motion-induced blur does not appear to be noticeable.

C. IR Airplane Images and Mirages

An IR image sequence for a regional jet taking off is shown in Fig. 7. In the first image (a), a modest mirage is apparent, with a slight appearance of a double-layer wing. This effect becomes much more pronounced in the second image (b), and even more so in the third (c). In fact, just before the airplane lifted off into the air, Fig. 7(c) shows a mirage in which almost the entire airplane thermal image was reproduced upside down, with the wheels lying in common in the right-side-up and upside-down images. The mirage features observed are very similar to what was observed nearly simultaneously on the VIS imagery [Fig. 6(d)].

Another airplane takeoff image sequence is shown in Fig. 8, but this time for a larger medium-range jet. These are similar to the VIS images in Figs. 6(a)–6(c). Again, inferior mirages are easy to detect, but this time the hot engines and wheels are even brighter than before. Similar to those in Fig. 7, the image in Fig. 8(a) shows the wheels being a common area in the original image and the mirage. However, different from the previous example, Fig. 8(b) shows a mirage in which the erect images of the wheels and the mirage wheels have separated.

The final example shown here is a regional jet landing (Fig. 9). The first image [Fig. 9(a)] was acquired just as the airplane touched down, so the

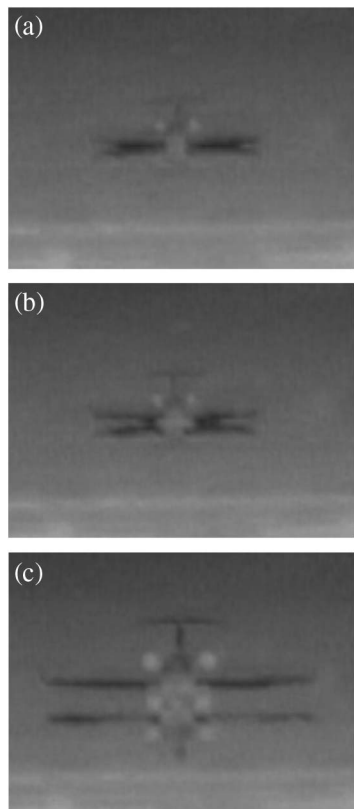


Fig. 7. LWIR images recorded during a regional jet takeoff [similar to Fig. 6(d)]. Inferior mirages are easy to detect. The image angular range is the same in all three IR images, but the image becomes larger as the airplane approaches the camera (Media 1).

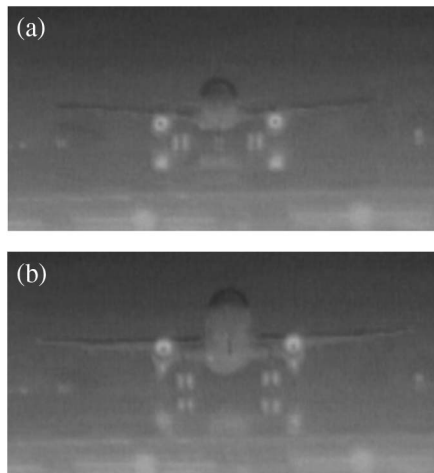


Fig. 8. Two still images during the takeoff of a jet [similar to Figs. 6(a)–6(c)] (Media 2).

wheels were still relatively cool. The rapid heating of the wheels immediately following touchdown is apparent in Fig. 9(b). The upturned wingtips are just resolvable in the airplane image, but are less apparent in the mirage.

To illustrate the dynamic nature of the IR mirages, a few thermal IR video sequences are also available online as supplements to this paper. These will allow the reader to watch the evolution of the airplane mirages at real speed. Media 1 shows a regional jet taking off. The plane turns onto the runway and immediately begins accelerating, at which time the engines become obviously hotter. As the airplane approaches closer to the camera, objects previously hidden below the vanishing line become apparent and one can observe a thermal image of the full airplane. This process appears almost as if the airplane is already rising into the air slowly, but in reality, it is still on the ground. As the airplane actually lifts off, the wheels and engines create an intriguing and rapidly

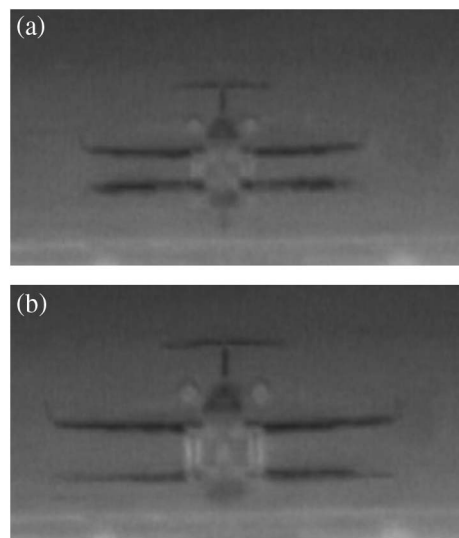


Fig. 9. LWIR images showing inferior mirages during jet landing (Media 3 and 4).

evolving mirage. A plume of hot gas becomes visible at the back of the engine on the right wing just before the plane flies out of the top of the image. For comparison, [Media 2](#) shows another takeoff of a medium-range jet with similar features.

Following the takeoff videos, [Media 3](#) shows a regional jet landing. The plane tips noticeably to its right side, causing the right wheel to touch the runway slightly before the left one. This causes the wheels to become bright, one after the other. Once on the ground, a mirage becomes immediately apparent, and evolves quickly as the plane brakes and slows down, all the while approaching the camera. The shimmering mirage again gives the appearance that the plane is repeatedly landing and taking off—ever so slightly. Finally, the plane turns toward the terminal building, giving the camera a great side view of the hot exhaust plume, with a barely visible mirage of the plume beneath the turning airplane. Finally, [Media 4](#) depicts a larger jet during landing. Although showing less-pronounced mirage features, this sequence nicely illustrates again how the wheels touch down one after the other, first on the sides and then the front wheels. The upper part of the hull nicely reflects the colder sky and the hot gas plumes from the turbine can be seen very easily when the plane turns sideways to the terminal.

5. Discussion and Conclusions

Examination of the refractive index of air in the VIS and IR leads to the conclusion that thermal IR mirages do occur with similar characteristics to VIS mirages, and without any noticeable dispersion effects that would give rise to spectral variation within the MWIR or LWIR bands. A telescope-mounted LWIR camera was used together with VIS cameras to record similar mirages of airplanes landing and taking off. All the usual mirage characteristics that are familiar in the VIS spectral range generally appear in the thermal mirages, except the thermal features arise primarily because of temperature differences, and secondarily because of emissivity differences and reflections.

We thank Polaris Sensor Technologies, Inc. (Huntsville, Alabama) for providing the IR telescope-mounted imaging system. This research was performed with funding from the U.S. National Science Foundation through Award ARC-1108427.

References

1. R. Greenler, *Rainbows, Halos, and Glories* (Cambridge University, 1980).
2. D. K. Lynch and W. Livingston, *Color and Light in Nature*, 2nd ed. (Cambridge University, 2001).
3. M. Vollmer, "Mirrors in the air, mirages in nature and in the laboratory," *Phys. Educ.* **44**, 165–174 (2009).
4. R. G. Greenler, "Laboratory simulation of inferior and superior mirages," *J. Opt. Soc. Am. A* **4**, 589–590 (1987).
5. C. Bohren, "Highway mirages," *Weatherwise* **42**, 224–227 (1989).
6. M. Vollmer and R. Tammer, "Laboratory experiments in atmospheric optics," *Appl. Opt.* **37**, 1557–1568 (1998).

7. W. H. Lehn and T. L. Legal, "Long-range superior mirages," *Appl. Opt.* **37**, 1489–1494 (1998).
8. C. H. Tape, "Aquarium, computer, and Alaska range mirages," *Phys. Teach.* **38**, 308–311 (2000).
9. M. Vollmer and R. Greenler, "Halo and mirage demonstrations in atmospheric optics," *Appl. Opt.* **42**, 394–398 (2003).
10. W. H. Lehn, W. K. Silvester, and D. M. Fraser, "Mirages with atmospheric gravity waves," *Appl. Opt.* **33**, 4639–4643 (1994).
11. A. T. Young, G. W. Kattawar, and P. Parviainen, "Sunset science. I. The mock mirage," *Appl. Opt.* **36**, 2689–2700 (1997).
12. W. H. Lehn, "Skerrylike mirages and the discovery of Greenland," *Appl. Opt.* **39**, 3612–3619 (2000).
13. J.-F. Baure, D. Clarke, P. Fuller, and M. Shough, "Unusual atmospheric phenomena observed near Channel Islands, UK, 23 April 2007," *J. Sci. Expl.* **22**, 291–308 (2008).
14. W. H. Lehn and W. G. Rees, "The Scoresby ship mirage of 1822," *Polar Rec.* **26**, 181–186 (1990).
15. A. B. Fraser, "Simple solution for obtaining a temperature profile from the inferior mirage," *Appl. Opt.* **18**, 1724–1731 (1979).
16. W. H. Lehn, "Inversion of superior mirage data to compute temperature profiles," *J. Opt. Soc. Am.* **73**, 1622–1625 (1983).
17. W. G. Rees, "Reconstruction of an atmospheric temperature profile from a 166-year old polar mirage," *Polar Rec.* **24**, 325–329 (1988).
18. W. G. Rees, C. M. Roach, and C. H. F. Glover, "Inversion of atmospheric refraction data," *J. Opt. Soc. Am. A* **8**, 330–338 (1991).
19. P. D. Sozou, "Inversion of mirage data: An optimization approach," *J. Opt. Soc. Am. A* **11**, 125–134 (1994).
20. R. Greenler, "Infrared rainbow," *Science* **173**, 1231–1232 (1971).
21. K. Mangold, J. A. Shaw, and M. Vollmer, "The physics of near-infrared photography," *Eur. J. Phys.* **34**, S51–S71 (2013).
22. M. Vollmer and K.-P. Möllmann, *Infrared Thermal Imaging—Fundamentals, Research and Applications* (Wiley VCH, 2010).
23. J. A. Shaw and P. W. Nugent, "Physics principles in radiometric infrared imaging of clouds in the atmosphere," *Eur. J. Phys.* **34**, S111–S121 (2013).
24. J. A. Shaw, P. W. Nugent, and M. Vollmer, "Infrared moon imaging for remote sensing of atmospheric smoke layers," *Appl. Opt.* **54**, B64–B75 (2014).
25. C. R. Zeisse, C. P. McGrath, K. M. Littfin, and H. G. Hughes, "Infrared radiance of the wind-ruffled sea," *J. Opt. Soc. Am. A* **16**, 1439–1452 (1999).
26. J. A. Shaw and J. H. Churnside, "Scanning-laser glint measurements of sea-surface slope statistics," *Appl. Opt.* **36**, 4202–4213 (1997).
27. J. D. Spinhire and T. Nakajima, "Glory of clouds in the near infrared," *Appl. Opt.* **33**, 4652–4662 (1994).
28. R. Feinberg and H. G. Hughes, "Marine boundary layer refractive effects in the infrared," *Appl. Opt.* **18**, 2532–2534 (1979).
29. R. N. Singh, S. S. Negi, A. K. Sahay, A. Singh, K. O. G. Varughese, and A. K. Walia, "Mirage formation in the thermal region," *Appl. Opt.* **33**, 3279–3280 (1994).
30. W. H. Lehn, "Analysis of an infrared mirage sequence," *Appl. Opt.* **36**, 5217–5223 (1997).
31. S. Church, "Atmospheric mirage and distortion modeling for IR target injection simulations," *Proc. SPIE* **2742**, 122–135 (1996).
32. K. Stein, "Investigations on the IR-range performance under different atmospheric conditions," *Proc. SPIE* **5981**, 59810A (2005).
33. G. J. Kunz, A. M. J. van Eijk, D. Tsintikidis, and S. M. Hammel, "Effects of atmospheric refraction and turbulence on long-range IR imaging in the marine surface layer: Comparisons between experiment and simulation," *Proc. SPIE* **5891**, 58910A (2005).
34. FeathIR Scope system by Polaris Sensor Technology, Inc., available at <http://www.polarissensor.com> (accessed 27 June 2014).
35. R. Penndorf, "Tables of the refractive index for standard air and the Rayleigh scattering coefficient for the spectral region between 0.2 and 20.0 μ and their application to atmospheric optics," *J. Opt. Soc. Am.* **47**, 176–182 (1957).

36. K. Edlén, "The refractive index of air," *Metrologia* **2**, 71–80 (1966).
37. P. E. Ciddor, "Refractive index of air: New equations for the visible and near infrared," *Appl. Opt.* **35**, 1566–1573 (1996).
38. G. Bönsch and E. Potulski, "Measurement of the refractive index of air and comparison with modified Edlén's formulae," *Metrologia* **35**, 133–139 (1998).
39. R. J. Mathar, "Calculated refractivity of water vapor and moist air in the atmospheric window at 10 μm ," *Appl. Opt.* **43**, 928–932 (2004).
40. R. J. Mathar, "Refractive index of humid air in the infrared: Model fits," *J. Opt. A* **9**, 470–476 (2007).
41. M. Vollmer, "Measuring distances in Google Earth," *Phys. Educ.* **48**, 145–149 (2013).